Article:

Geddes, D.A., Walkley, B. orcid.org/0000-0003-1069-1362, Matsuda, T. et al. (1 more author) (2024) Multi-year cementitious hydrate product formation in non-Portland high performance concretes. CEMENT. 100111. ISSN 2666-5492

https://doi.org/10.1016/j.cement.2024.100111

Cement 18 (2024) 100111

Contents lists available at ScienceDirect

Cement

journal homepage: www.sciencedirect.com/journal/cement

Multi-year cementitious hydrate product formation in non-Portland high performance concretes

Daniel A. Geddes [a], Brant Walkley [a,b], Taku Matsuda [c], John L. Provis [a,d,*]

[a] Department of Materials Science and Engineering, University of Sheffield, Sir Robert Hadfield Building, Mappin Street, Sheffield, S1 3JD, UK
[b] Department of Chemical and Biological Engineering, University of Sheffield, Sir Robert Hadfield Building, Mappin Street, Sheffield, S1 3JD, UK
[c] R&D Center Technological Department Division, Sumitomo Mitsui Construction Co., Ltd, Nagareyama-Shi, Chiba, 270-0132, Japan
[d] Paul Scherrer Institut, Laboratory for Waste Management, Forschungsstrasse 111, 5232 Villigen PSI, Switzerland

ARTICLE INFO

Keywords:
Chemically-activated binders
Supplementary cementitious materials
High-performance concretes
Spectroscopy

ABSTRACT

This paper describes the hydration products and microstructural formation processes that yield excellent mechanical properties in “zero-cement concretes” (ZCC) produced by chemical activation of a blend of silica fume, blast furnace slag, and fly ash, using a CaO-rich additive (commercially supplied as an expansive agent but taking a chemical activation role here), a high superplasticizer dose, and a very low water content. These concretes reach 70 MPa at 28 days and then continue to gain strength beyond 150 MPa after 5 years, either under sealed conditions or exposed on a rooftop in the climate of Tokyo, Japan. The reaction products of ZCC are dominated by C-A-S-H gel, accompanied by aluminate hydrates of different layered double hydroxide forms; this unconventional cementitious blend yields reaction products that are familiar from Portland cement and blended binder systems. The ferronickel slag used as fine aggregate in these mixes makes an important contribution to the balance of fresh-state and hardened-state properties by modifying hydration chemistry.

1. Introduction

The sustainable development of current and future global infrastructure will require concretes of varying performance levels, each produced in the most environmentally efficient manner and with maximum re-use of industrial by-products and wastes in concrete production [1]. The particular focus of this paper is on concretes of very high compressive strength, which can be valuable in reducing material demand to achieve given levels of structural performance for very efficient design of buildings, bridges and other important infrastructure elements [2]. Conventionally, high-performance concretes have been produced using high contents of Portland cement, which brings a significant Greenhouse emissions footprint [3]. In some cases this high cement content is more than compensated by improved performance metrics, which mean that high-strength materials may be the most environmentally efficient way to deliver structural elements for a specified purpose [2,4].

The use of “high-performance” as a descriptor for concretes was originally largely related to mechanical strength, but has been expanded to also include aspects of durability, as the very low water/cement ratio that is used in many high-performance concretes brings a low volume and low connectivity of the pore space. These characteristics are highly beneficial in preventing transport of potentially aggressive agents (e.g. chloride, carbonate, sulfate) from the environment into the concrete, and can therefore aid in providing a very extended service life.

Recent research and development efforts focused on both conventional and high-performance concretes seek both strength and durability at minimized Portland cement content. As a particular embodiment of this ideal, it has been demonstrated through the development and commercialization of a class of products named “Sustain-crete” (STC, https://www.smcon.co.jp/en/technology/sustain-crete/)” [5-11]. In this paper, a type of STC that does not containing Portland cement is referred to as Zero Cement Concrete, "ZCC". ZCC has excellent concrete performance in both fresh and hardened states, which can be achieved through appropriate design of reactive powder blends that contain no Portland cement, at a very low water/binder ratio, enabled through triggered release of a sorbed superplasticizer from silica fume through addition of a calcium-rich expansive additive which also chemically activates the siliceous powders [12]. The ZCC mixes discussed here are based on a ternary cementitious blend of silica fume (SF), ground granulated blast furnace slag (BFS), and fly ash (FA). The principles of the ZCC product family have been shown to offer the possibility of very

---

* Corresponding author.
E-mail address: john.provis@psi.ch (J.L. Provis).

https://doi.org/10.1016/j.cement.2024.100111
Received 27 December 2023; Received in revised form 18 June 2024; Accepted 29 August 2024

high strength, ongoing strength development in service over a period of multiple years, and excellent dimensional stability (very low and controllable shrinkage) [5,7-10]. These concretes have also been shown to give attractive engineering performance when used in combination with steel fiber reinforcement for structural applications [13]. Fig. 1 shows an example of the type of structural element that can be produced using ZCC, with the excellent surface finish showing evidence of very good fresh-state properties, and the measured compressive strength of 150 MPa at 6 days (achieved using steam curing) offering an appealing possibility for the design of slim and efficient structures.

A key question related to the longer-term development of the mechanical properties of a cementitious material is whether the mechanism of the initial reaction (or activation, in this case) process yields a microstructure with characteristics suitable for later reaction to continue and a high degree of reaction to eventually be obtained. For example, activation of blast furnace slag by sodium silicate involves hydrate product growth initially in a way that does not block the slag particle surfaces, yielding a microstructure in which the activator can continue to access slag grain surfaces long after hardening and meaning that the binder can continues to evolve and gain mechanical properties for an extended period [15,16]. Conversely, the use of NaOH as an activator gives high early strength, but a microstructure with dense shells of reaction products surrounding the remnant slag grains which restricts ongoing reaction and later strength gain [16,17]. Considering ZCC as a chemically-activated binder, with its reactions initiated and promoted in particular by the CaO supplied by the expansive additive, and in the absence of extensive literature specific to CaO-SF-BFS-FA binding systems, it is useful to consider microstructural parallels with other related binder types in this way. The concepts discussed here are also developed with consideration of past investigation of the CaO-PC-SF-BFS binding system by Seo et al. [18], but the absence of PC in the ZCC samples here does raise important mechanistic differences at early age.

In advancing the practical uptake of these materials, given that they do not contain conventional Portland cement, it is essential to fully understand their phase assemblages and microstructure, to gain confidence in their long-term performance. Preliminary results have shown very good stability (and ongoing development) of engineering properties over periods of up to two years in natural environmental conditions [7], but the key focus of this paper is to provide analysis of the fundamental physicochemical basis of the high strength and durability of ZCC binders. This will be achieved through testing and analysis of the materials themselves, and in particular through developing parallels between the phase assemblages that are identified in ZCC and those which are well known and understood to give excellent durability in conventional Portland and blended cements. The core research questions to be addressed are:

- Which phases form in the ZCC binder, and when do they form?
- How do these hydrate phases combine with each other, and with the fine aggregate in particular, to yield a microstructure which shows such high performance?

2. Experimental procedure

2.1. Materials

The basic characteristics of the raw materials used are presented in Table 1. All materials were supplied by Sumitomo Mitsui Construction Corporation for use in this research.

Concrete mix designs are outlined in Table 2. A ferronickel slag-derived fine aggregate (FNS), with density of 2.92 g/cm^3 and water absorption of 2.64 %, was used. The coarse aggregate (CA) was a crushed hard sandstone, with density of 2.64 g/cm^3 and water absorption of 1.24 %. A polycarboxylate-based superplasticizer (abbreviated SP; Sikament 1200 N, Sika Ltd., Japan; Mw = 18 kDa) and a CaO-type high early strength expansive additive (abbreviated EX; product name

Table 1
Raw material oxide compositions, as determined by X-ray fluorescence. All values in wt.%.

	Fly ash (FA)	Ground granulated blast furnace slag (BFS)	Silica fume (SF)	FNS
SiO_2	60.2	32.3	94.0	49.9
Al_2O_3	24.0	14.3	0.5	2.4
CaO	2.7	43.0	0.3	2.5
Na_2O	0.5	0.3	0.4	0.1
MgO	1.6	6.5	0.5	32.3
Fe_2O_3	4.6	0.6	1.5	7.9
TiO_2	Trace	trace	trace	2.3

Fig. 1. In-service example of a 150 MPa Zero Cement Concrete element being used to construct a bridge [14]. The material depicted, marketed as "Sustain-Crete", is a commercial product resulting from the lines of research and development described in this article and using the same mix design principles.

Table 2
Concrete mix design (all quantities in kg/m^3 unless otherwise noted).

Water	SF	FA	BFS	EX	FNS	CA	Air (vol.%)	Total binder	w/b (-)
89	84	168	307	20	1073	779	3.5	579	0.155

N-EX from Taiheiyo Materials Corporation) were added. The supplier data sheet available for the N-EX product declares a CaO content (as free lime) of 55 (±5) wt.%, along with 25 (±5) wt.% $CaSO_4$ (as anhydrite), with the balance hydraulic calcium silicates and aluminates.

2.2. Sample preparation

The mixes defined in Table 2 have been produced by incorporating the CaO-type expansive additive as a chemical activating agent, blending this into the dry mix using a high shear mixer. The water and superplasticizer (at a dose of 1.3 % relative to the binder) were then added to the mix, which was sheared at 2000 RPM. The paste and mortar samples were then sealed and stored in a controlled environment at 20 °C.

Concrete specimens were produced using an industrial high-shear mixer in batches of 100 L, cast into steel molds, demolded at 2 days, then cured under three sets of conditions until testing:

- Sealed in polymeric wrap at 20 °C
- Wet-cured under water at 20 °C
- Exposed on a rooftop in the Tokyo region, Japan (Köppen climate classification *Cfa*, humid subtropical)

Mechanical properties were determined according to Japanese standard methods using triplicate cylinders of ø100×200 mm: JIS A1108 for compressive strength, JIS A1113 for splitting tensile strength, JIS A1149 for static elastic modulus. The Poisson's ratio was obtained by measuring the strain in the direction perpendicular to the loading direction when measuring the static elastic modulus according to JIS A1149, and calculating the ratio of the two.

Paste specimens were produced for instrumental analysis according to the same mix designs as the concretes (Table 2) by simply omitting the fine and coarse aggregates from the formulations described; no adjustment to water content was made in producing pastes. Pastes were mixed using an overhead mixer and high-shear blade, then poured into sealed tubes for curing at 20 °C until testing. Similarly, mortars were formulated by simply omitting the coarse aggregate, and were produced in a planetary mixer, cast in 50 mm cube molds, demolded after 3–7 days, and then sealed in polyethylene bags and cured at 20 °C until testing.

2.3. Analytical techniques

Scanning electron microscopy (SEM) of mortars was conducted on a Hitachi TM4040 instrument, with an accelerating voltage of 15 kV. Energy dispersive x-ray (EDX) analysis was performed using a Bruker Quantax detector.

Mercury intrusion porosimetry (MIP) has been used to analyze the pore size distribution and total porosity of mortar samples that were cast and cured in parallel with the long-term concretes. The samples were cut into uniform size pieces, solvent exchanged in isopropanol, and then dried under vacuum. An Autopore IV porosimeter (Micromeritics) was used to introduce mercury into the sample, to a maximum pressure of 413 MPa.

To determine the kinetics of formation of the cementitious gel structure, isothermal conduction calorimetry has been performed for pastes using an 8-channel TA Instruments TAM Air calorimeter at 20 °C, using an external mixing protocol.

Leaching experiments were performed on the aggregates by immersing them in saturated solutions of $Ca(OH)_2$, or 1 mol/L NaOH, at 25 °C. The samples were filtered to remove the leachate from the aggregate and the resulting solution was analyzed using ICP-OES to determine the concentrations of elements removed from the aggregate. This test was used to determine any possible contribution of reactive constituents of the aggregates in the hydration processes.

Solid state single pulse ^{29}Si and ^{27}Al magic angle spinning (MAS) NMR data were obtained to examine the local structure of the reaction products in paste samples. All ^{29}Si and ^{27}Al spectra were acquired at 11.7 T on a Bruker Avance III HD 500 spectrometer operating at Larmor frequencies 99.35 MHz and 130.28 MHz, respectively. A Bruker 4.0 mm dual resonance CP/MAS probe was used enabling a MAS frequency of 12.5 kHz. ^{29}Si MAS NMR spectra were acquired using a 5.5 μs $\pi/2$ excitation pulse, a measured 90 s relaxation delay, a total of 256 FIDs per spectrum. ^{1}H-^{29}Si cross-polarization (CP) MAS NMR experiments were performed using a ^{29}Si $\pi/2$ pulse width of 1.7 μs, an initial ^{1}H non-selective ($\pi/2$) pulse width of 2.5 μs, a recycle delay of 1.5 s and a contact pulse of 1.7 ms. A nominal ^{1}H decoupling field strength of 80 kHz was employed during acquisition and 10,240 transients were collected per experiment. ^{27}Al MAS NMR data were acquired using a 1.7 μs $\pi/2$ excitation pulse, a measured 10 s relaxation delay, and a total of 64 FIDs per spectrum. A Bruker 4.0 mm dual resonance CP/MAS probe was used, enabling a MAS frequency of 12.5 kHz. For ^{29}Si and ^{27}Al, pulse calibration and chemical shift referencing were carried out using the IUPAC primary references pure tetramethylsilane (TMS) (δ_{iso}= 0 ppm) and 1.0 M aqueous $NaCl_{(aq)}$ (δ_{iso}= 0 ppm), respectively.

Synchrotron radiation Fourier transform infrared (SR-FTIR) microscopy was conducted using the B22 instrument at the Diamond Light Source facility [19]. Multispectral images were collected for polished cementitious paste and mortar samples using a Hyperion 3000 microscope with synchrotron radiation, an energy range of 4000 to 700 cm^{-1}, with a step size of 20 μm, and a beam spot size of 10 μm controlled using aperture slits.

3. Results and discussion

3.1. Development of mechanical properties, and a hypothesis regarding reaction mechanisms

Fig. 2 shows that the compressive and tensile strengths of these samples are very high, and particularly highlights the fact that compressive strength and elastic modulus (and therefore presumably also splitting tensile strength, although experimental data were not available for that parameter) continue to increase over time up to 5 years of curing under all conditions tested. By comparison, a parallel set of high-performance Portland cement concretes produced and cured under the same conditions, using plain Portland cement at $w/c = 0.36$ [9], had very similar 28-day and 56-day compressive strengths of approximately 70–75 MPa to match the ZCC mixes, but then gained only 15 % additional strength up to 5 years, compared to the 100 % strength increase observed in this time period for ZCC.

So, it is valuable to understand the reaction processes and mechanisms which are contributing to this excellent performance. The concept of the gel-space ratio [20-22] has long led researchers to understand that the most direct way to gain strength in designing a cementitious material is to fill as much of the interstitial space as possible with hydrate phases. The ZCC samples studied here, which have water/binder (w/b) ratios far below the values that are conventionally defined as being needed for full hydration of Portland cement (although such calculations are far from straightforward for these complex blended non-Portland binders), clearly have the opportunity to benefit from a very high gel/space ratio as an excellent starting point for high strength development.

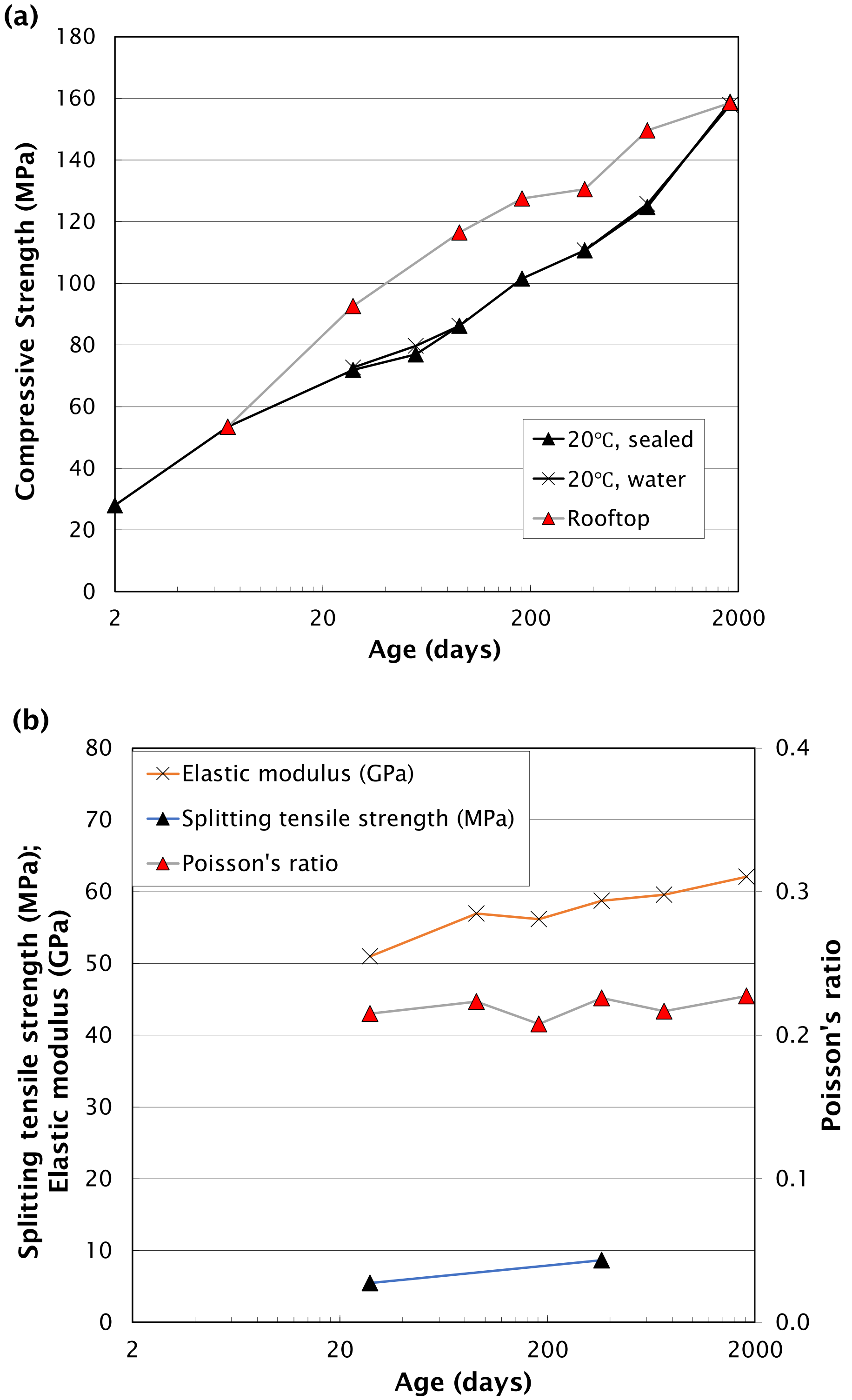

Fig. 2. Evolution of mechanical properties of ZCC, for ages up to 5 years. (a) Compressive strength under different curing conditions; the data for sealed and water-cured samples are overlaid upon each other at most ages. (b) Splitting tensile strength, elastic modulus, and Poisson's ratio for samples cured sealed at 20 °C. A representative experimental error bound is ±3 MPa on compressive and splitting tensile strength data points, ±5 % on elastic modulus, and ±10 % on Poisson's ratio. Data for ages up to 1 year were published in [9].

However, it is also essential to ensure that hydration processes are able to fill in the space effectively, and that the essential strength-giving reactions are not hindered or halted by microstructural blocking effects. Very low-w/b pastes often have low degrees of hydration and restricted hydration product formation because of hydrate shells blocking the surfaces of cementitious particles and preventing further reaction [23-25]; it is therefore important to investigate if a similar phenomenon may be somehow restricting ongoing strength and microstructural development in the ZCC samples studied here. The data in Fig. 2 indicate *prima facie* that this is unlikely to be occurring, because the compressive strength evolution under each curing condition depicted is continuous and monotonic up to 5 years of age. The apparent upward curvature in the data sets for both sealed and water curing (which are remarkably similar to each other) is to some degree an artefact of their depiction on a semi-logarithmic plot, but the fact remains that the reactions are clearly continuing to contribute strength-giving microstructural features over a very extended time period. There is also a ~70 % increase in the splitting tensile strengths of sealed-cured ZCC specimens from 28 to 365 d, which is consistent with the compressive strength evolution shown in Fig. 2. As was discussed in previous work using earlier-age data sets for these samples [9], both the splitting tensile strength and elastic modulus data fall close to the upper bound of values within a large collected database correlating these parameters to concrete compressive strengths [26,27], and the later-age elastic modulus data that have been collected and presented here are consistent with this observation.

It is therefore important to develop and present a hypothesis regarding the microstructural and chemical development of ZCC, which will then be tested and refined through the remaining sections of the paper.

The chemical mechanisms that drive the setting and hardening of ZCC will initially be based around alkali-earth activation of highly reactive pozzolanic constituents (i.e. the reaction between CaO from the expansive additive, water, and silica fume, in the samples studied here), at a low w/b ratio that is enabled by the timed release of polycarboxylate superplasticisers from the surface of the silica fume particles to fluidise the mix [12]. Later in the reaction process, the moderately-reactive BFS constituent of the mix will begin to make an important contribution to microstructural evolution; this is less dependent on the provision of calcium hydroxide to enable its conversion to C-A-S-H, as the latent hydraulic character of the BFS enables the reaction to proceed.

Considering in turn the different potentially cementitious constituents of the ZCC binder formulation, it is clear that the initial reaction will involve the dissolution of the expansive additive, which will generate a sufficiently high pH (expected to be >12, although not able to be directly measured in these concrete mixes) to trigger the dissolution of the silica fume as the most reactive cementitious powder present. This will be accompanied by release of the polycarboxylate superplasticizer from the silica fume particles as was discussed in detail in [12], which is not particularly the focus of the current discussion as the direct (chemical) contribution of the polycarboxylate to microstructural development is at most a secondary effect.

If it is assumed, as the foundation of the hypothesis to be tested here, that the silica fume particles are well dispersed in the interstices between fly ash and slag grains, this would lead to initial C-S-H formation (by reaction between CaO from the dissolved expansive additive, and SiO_2 from the silica fume) in these regions which would conventionally be considered to be the "outer product" regions of a cementitious microstructure, rather than on or near the BFS and fly ash surfaces. So, despite the very low water content of these binders - which is at a level that in conventional ultra-high-performance concretes may be expected to lead to a congested microstructure and a large degree of surface blockage – it is in fact expected that the BFS grains, which are the next-most-reactive solid constituent after silica fume, would thus be able to react in a latent-hydraulic mechanism, relatively unimpeded by previously formed C-S-H. This reaction will take place in the presence of a significant concentration of sulfate supplied by the expansive additive (considering its high solubility and the very low free water content), and so would be expected to yield some calcium sulfoaluminate hydrates in addition to the Al-substituted C-S-H type gels. The fly ash is the least-reactive constituent of the powder blend and would be expected to contribute relatively less to the hydration process in the first days or weeks after mixing; this may contribute later in the reaction sequence, but its primary role at early age is probably as a filler.

The exact nature of the reaction products formed at different ages, and through the successive reactions of the three cementitious powders, will be explored in detail through spectroscopic techniques in the subsequent sections of this paper. However, before investigating these questions at a chemical level, it is important to analyse the microstructure of ZCC paste as it hardens and continues to gain strength, to test the hypothesis presented in the paragraphs above.

3.2. *Porosimetry*

The first step in understanding the ZCC microstructure is to characterise the pore volumes of these materials, to determine whether the capillary pore structure is coarse (as characterises NaOH-activated BFS binders with poor longer-term strength gain) [17], or whether the separation of initial reaction products forming away from BFS surfaces can in fact yield a highly refined pore structure and enable a higher degree of reaction to be approached.

Fig. 3 shows mercury intrusion porosimetry (MIP) data for ZCC concrete samples (mix designs as shown in (Table 2) at different ages and under different curing conditions. The intrusion plots show some pores registering at larger pore diameters (> 10 μm), but pores in this size range were not evident in any of the scanning electron microscopy (SEM) imaging conducted for these samples, which will be presented below. These pores are thus described as an experimental artefact in the MIP data, attributed to inter-particle voids in the crushed test samples and potentially some cracks induced by the sample preparation process. The samples tested by MIP were sourced from compressive test cylinder specimens after crushing for strength determination, which were further mechanically size-reduced to an appropriate size for MIP analysis. For this reason, the pores > 1 μm have been shaded in grey in Fig. 3 and will not be the focus of the analysis presented here.

The data show that there are only minor differences in overall porosity; these differences are in most cases within the uncertainty bounds of duplicate tests for samples exposed to the same curing conditions. The main exception to this trend is for the sample that had been exposed for two years under the Rooftop conditions (i.e. outdoors, exposed to the hot summers and cool winters of Tokyo, with plentiful rainfall and generally relatively high humidity). This sample showed a low porosity consistent with its higher strength development, which may be connected to a higher extent of reaction as Tokyo's climate provided both a warm environment and sufficient moisture to enable the latent hydraulic slag reactions to continue. Fig. 3 shows that the volume of ~50 nm pores is significantly reduced as the Rooftop sample ages for up to 2 years, which is fully consistent with the hypothesis of ongoing reaction of the aluminosilicate cementitious constituents (BFS then FA) under a continued supply of water, generating cementitious hydrate products that contribute to microstructural refinement and strength gain.

The comparison between the three curing conditions shown in Fig. 3 for samples at 720 days of age shows a strikingly lower measurable porosity, which correlates with the higher measured compressive and splitting tensile strengths, for the Rooftop sample than when curing is conducted under sealed or immersed conditions. This may logically be connected to microstructural evolution leading to pore refinement and thus a higher gel-space ratio as discussed in Section 1. However, comparing the results presented in Figs. 2 and 3 for the Rooftop samples at 28, 365, and 730d, it is clear that the MIP data alone are not sufficient to explain the change in strength. Fig. 3 shows very similar total pore volumes at 28 and 365 d, but Fig. 2 shows that the compressive strength increased by ~30 % during this time; this lack of a direct correlation is highlighted in Fig. 3b. Although the MIP instrument used here is able to probe pores with entry diameters as small as 2 nm, it is possible that some fraction of the pores in the Rooftop 730 d sample have either become disconnected from access via the surfaces of crushed particles, or refined into diameters below the measurable size range, rather than being closed entirely. This is consistent with a comparison of the evolution of the shapes of the MIP curves in Fig. 3a as a function of time, which indicate that pore refinement accompanies strength increase in this sample.

These results therefore indicate that the ZCC materials appear to be behaving in accordance with the established theory and understanding

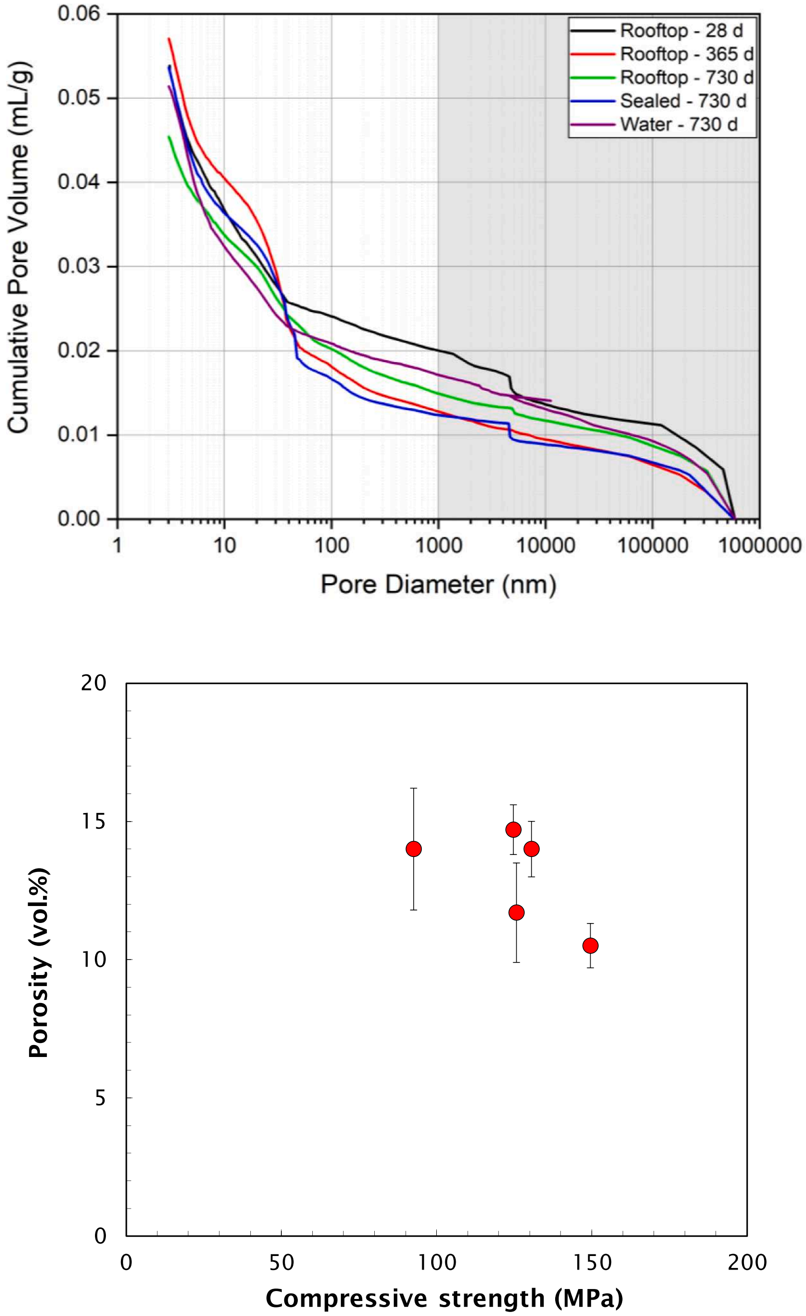

Fig. 3. (a) Mercury intrusion porosimetry data for mortar samples cured and exposed to accompany the concretes [7], and (b) comparison between compressive strength (from Fig. 2a) and total measured porosity (from Fig. 3a) for the same subset of samples as shown in Fig. 3a. Pores in the size range >1 μm, shaded grey in Fig. 3a, are assigned to cracking of the samples during mechanical size reduction and are excluded from the analysis.

of Portland cement-based materials in terms of the relationship between pore structure, porosity, and strength, although with a much greater proportion of the strength being gained at later ages (more than doubling from 28 d to 5 years under sealed conditions, Fig 2a) than is common for Portland cement-based HPC [5,28]. To understand the reasons for this behavior, it is important to next investigate the microstructural development of the ZCC binder and mortar.

3.3. *Microstructural development*

ZCC has been shown to have a very high tensile and compressive strengths, as discussed above; the core reasons underpinning the development of this strength must be linked to details of the microstructure. The microstructural aspects that can be viewed by SEM are in good agreement with the porosimetry data (Section 3.2) which show a dense matrix of low porosity; the images in Fig. 4 also show high matrix density, whilst also showing good particle adhesion, evidenced by a lack of separation at particle-gel boundaries and very low cracking induced by the polishing and imaging process. The extent of reaction visibly varies between the residual particles shown embedded in the binders in Fig. 4, with quite some predominance of unreacted fly ash and slag grains in the microstructure, particularly in the 7 d image in Fig. 4a. This

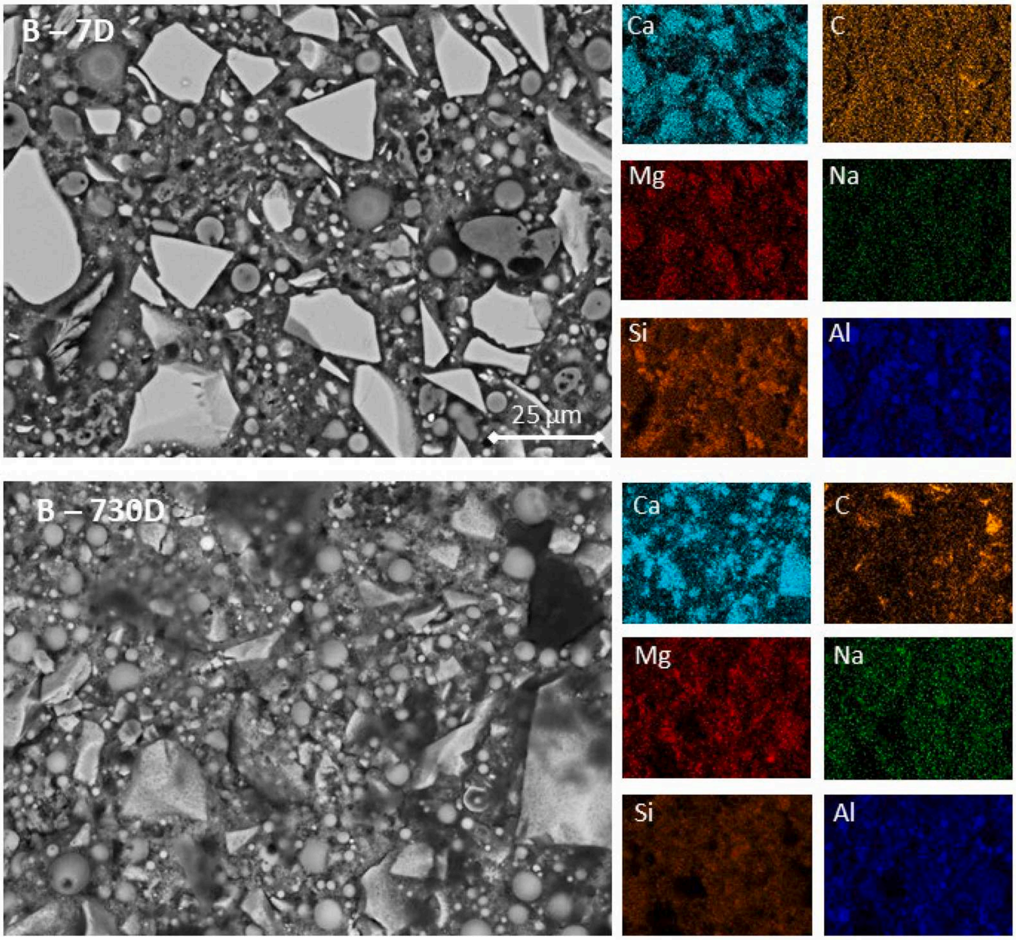

Fig. 4. - Scanning electron micrographs showing the pore structure and composition of ZCC paste with CaO expansive additive at 7 and 730 days of curing. Accompanying elemental maps are shown for Ca, Mg, Si, C, Na and Al. The scale bar shown in the upper micrograph applies also to the lower.

is consistent with the hypothesis raised above, that much of the binder that has formed in the first weeks of hydration is attributed to the pozzolanic reaction of the silica fume (which is present as particles too small to observe directly by SEM at the magnifications accessible here), with a lesser contribution from BFS hydration. The BFS grains may be showing some evidence of reaction rims at 730 d, and a minority of the fly ash grains also show evidence of having undergone some reaction at this age. There is some evidence of superficial carbonation in the 730 d sample evidenced in the EDX spectrum, which is likely to have taken place during sample preparation for microscopic imaging and should not be considered to be an intrinsic feature of ZCC; these materials have previously shown very good carbonation resistance under accelerated testing [5].

Overall, the structural features of ZCC as evidenced by Fig. 4 appear

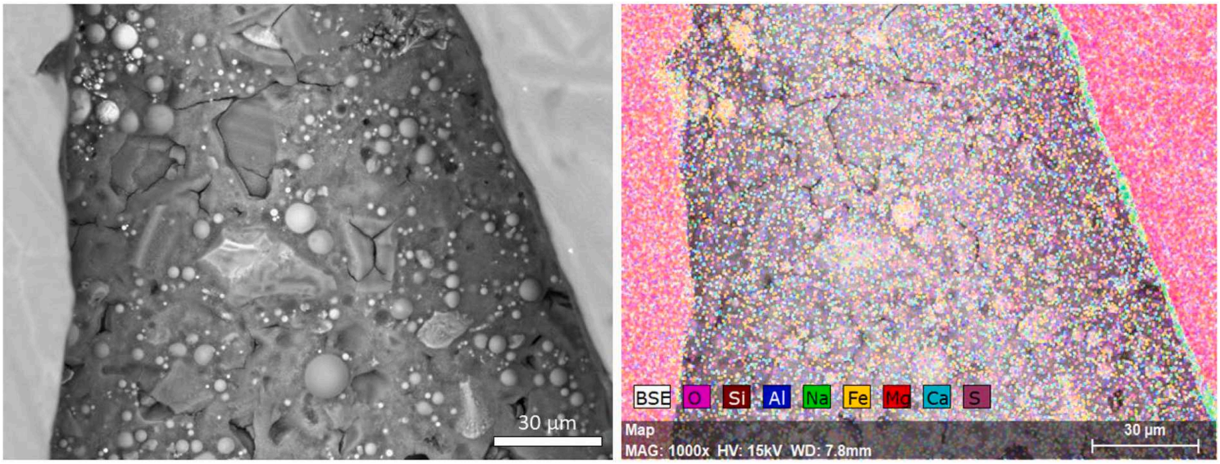

Fig. 5. SEM image and corresponding EDX elemental map of a 28-day cured ZCC mortar with FNS aggregate, showing the microstructure of the ZCC paste in between two FNS aggregate particles.

to be very similar to the assemblages of unreacted BFS and FA grains embedded in C-A-S-H gels in comparable PC-BFS-FA ternary binders [29]. Formation of a C-A-S-H gel network at early age by SF reaction in a location separate from the BFS particle surfaces has, as hypothesised in Section 3.1, provided the opportunity for a dense microstructure via relatively unhindered (considering the very low water content of the pastes) ongoing reaction processes. The CaO constituent of the expansive additive activates the paste via a process with parallels to lime-pozzolan reactions in conventional and also historic binder materials [30], which will be demonstrated and discussed in detail below.

SEM imaging of mortars, Fig. 5, provides further evidence for the basis of the excellent splitting tensile performance of ZCC, showing very strong adhesion between the main C-A-S-H gel binding phase and the visible unreacted particles (slag, fly ash, FNS aggregate) in ZCC. This is attributed to chemical bonding interactions at the respective interfaces, where the slag and fly ash particles are reactive as binder-forming constituents, and the FNS used as fine aggregate here is also partially reactive at its surface [31-33]. The presence of a high level of fly ash within the binder formulation has previously been shown to mitigate any possibility of alkali-silica related expansion processes in Portland cement-based binders containing FNS fine aggregate [33], and none of the ZCC specimens produced in this and related investigations have shown any indication of degradation due to alkali-silica reactions under laboratory or exposed conditions, so it appears likely that this slight degree of reactivity at the aggregate particle surfaces will have a beneficial rather than detrimental effect on material properties. In a previous study using a different FNS aggregate, Nguyen et al. [31] made use of this surface reactivity to densify the interfacial transition zone and improve tensile properties of their Portland cement-based concrete formulations, and it is expected that the FNS used here is providing a similar performance benefit.

The paste microstructure shown in the backscattered electron image in Fig. 5 provides further evidence that the reaction is able to proceed effectively and to a high degree, even with a very low water/cement ratio. As observed above related to Fig. 4, the BFS particles shown in Fig. 5 (e.g. the angular grain at top/center of the image) are reacted to a high extent, and show the characteristic concentric-rings structure that is associated with well-reacted slag grains [15,34]. The ring structures display both chemical and density zonation, with varying degrees of intermixing of C-A-S-H and Mg-Al LDH phases [35]

The extent of reaction of the fly ash grains appears from these images to be relatively low, and the incremental contribution of the fly ash to compressive strength gain from 28 to 204 days was previously shown (by comparison of ZCC mixes with and without FA) to be limited [9]. The fly ash seems to contribute to the material and microstructural formation mainly via improving flow characteristics in the fresh state [9], consistent with its role in Portland cement-based binders [36-38]. However, the presence of fly ash has been identified to be important for the long-term evolution of splitting tensile strength in ZCC [9], which leads to the suggestion that these hard and stiff particles, with reactive surfaces, are acting as a tightly-bound micro-aggregate where the strong adhesion of the paste (mainly resulting from reaction of SF and BFS) to the FA particle surfaces (in addition to the surfaces of the FNS and potentially also the conventional aggregate grains) is contributing to the high tensile performance of the materials.

Any discussion of interfacial transition zone effects around aggregates is complex [39], particularly where non-conventional binders are used [40], and depend on casting orientation [41], which was unfortunately not able to be accurately tracked for these samples during their preparation for SEM imaging. There is an apparent sodium-rich region near the surface of the right-hand aggregate grain in Fig. 5b (appearing as a green line in the EDX map). This may at first glance be assumed to represent a region of higher porosity, with sodium being associated with the pore solution, as is seen in many alkali-activated binders. However, the low paste alkali content in these CaO-activated binders, and the excellent flexural performance of the ZCC specimens [9], combine to indicate that it is very unlikely that a weak and porous ITZ is being observed here, and so this elevated sodium concentration at the aggregate-paste interface must be sought. Leach testing of the FNS aggregate in saturated $Ca(OH)_2$ solution showed measurable release of Na under those conditions, particularly from 14 to 90 days of exposure of the aggregates to an alkaline environment, which is consistent with the suggestion that the Na enrichment is related to some degree of aggregate reaction – hence potentially involving some binding to the paste – rather than indicating a porous region forming within the binder.

3.4. Phase evolution and reaction pathways

It is clear from the discussion above that more insight into the microstructural evolution and phase formation, in both paste and mortar samples, is necessary to more fully test the reaction pathway hypotheses presented above. For this reason, various aspects of the ZCC formulation were tested by isothermal calorimetry:

- ZCC paste, consistent with the experimental work on pastes presented in the preceding sections
- ZCC mortar with the FNS fine aggregate shown in Fig. 5 (denoted FNS-1), which has 3 % water absorption and moderately rough surface texture on the particles
- ZCC mortar with a conventional hard siliceous sand fine aggregate (denoted HS)

The data for the paste in Fig. 6 show a small peak at 0.5 days and a larger one at 1.5 days. The onset time of the more intense (the latter) of these peaks is unchanged by the addition of conventional siliceous sand, but this sand suppresses the smaller first heat release peak. Conversely, the FNS fine aggregate enables the first small heat release peak to be retained, but slightly delays the onset of the second peak. The overall profile of the main peak at 1–2.5 days is largely unchanged by the addition of either of the sands, despite the retardation of this peak due to the FNS. Connecting to the discussion above, and previous observations from Nguyen et al. [31] that the interfacial transition zone in Portland cement-based binders around FNS particles shows a reduced portlandite content compared to the corresponding zone with conventional sand, it appears that the surface reactions of the FNS are consuming some of the reactive ions provided by the reacting precursor blend into the pore fluid, which delays the reaction slightly until precursor dissolution proceeds further. Isothermal calorimetric analysis of the ZCC paste

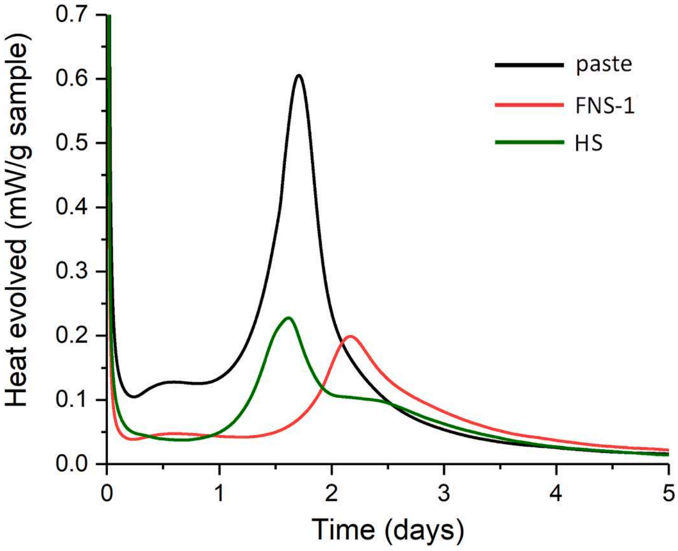

Fig. 6. Isothermal calorimetry data for selected ZCC paste and mortar specimens.

without addition of the CaO-rich expansive additive (not shown in Fig. 6) showed essentially no heat release, consistent with the discussion above that the CaO is essential to chemically activate the precursors, in addition to its role in triggering the superplasticiser release from the SF particles as discussed in detail in [12].

It is also important to understand the bulk phase formation among the hydration products of ZCC. For this purpose, X-ray diffraction analysis is presented in Fig. 7 for a ZCC paste as a function of sealed curing time. These data show relatively little change in the phase assemblage from 3 to 180 days, with a broad feature around 30° 2θ due to early C-S-H formation, continuing to grow up to 730 d as this evolves into C-A-S-H via later BFS and FA reaction. Some ettringite forms at early age as the sulfate supplied by the expansive additive reacts rapidly with Al from the BFS, and persists up to 730 d although with some apparent fluctuation (e.g. the ettringite content seems lower in the 180 d sample than at other ages, which may be a sample-level variation); this observation will be revisited in Section 3.5 in the discussion of NMR spectra. The content of quartz and mullite, which are attributed to the residual fly ash particles, vary somewhat between time points because these phases tend to be present as relatively large crystals that are to some degree heterogeneously distributed throughout the samples. These phases are not considered to be reacting to any significant extent, consistent with the extensive body of literature related to fly ash reaction in blended and alkali-activated cements. A small amount of calcite formation is again attributed to superficial carbonation of the samples during preparation and analysis.

It should be noted that there is no evidence, even at 3 days, of any residual particles of the expansive additive persisting within the hardened binder. This is important because later-age hydration of any remaining free lime may raise a risk of deleterious expansion and cracking, but the data presented here show that this is fully consumed in the early stages of reaction, which is attributed to the high content and reactivity of the silica fume constituent of the ZCC.

3.5. *Binder chemical structure and spectroscopic analysis*

The ^{29}Si MAS NMR data (Fig. 8) of each sealed-cured paste sample indicate the formation of reaction products with Si environments resonating at an isotropic chemical shift, δ_{iso}, = −75 ppm, −80 ppm, and −85 ppm. These resonances are attributed to Q^1, Q^2(1Al), and Q^2 sites

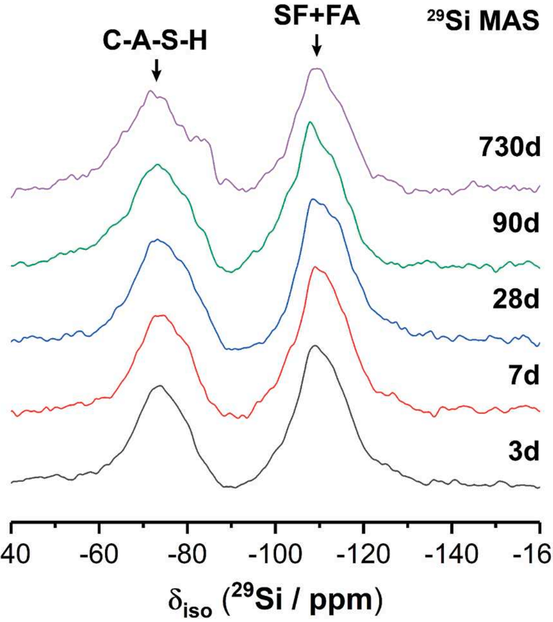

Fig. 8. ^{29}Si MAS NMR spectra of ZCC pastes, as a function of sealed curing duration; includes some data from [10].

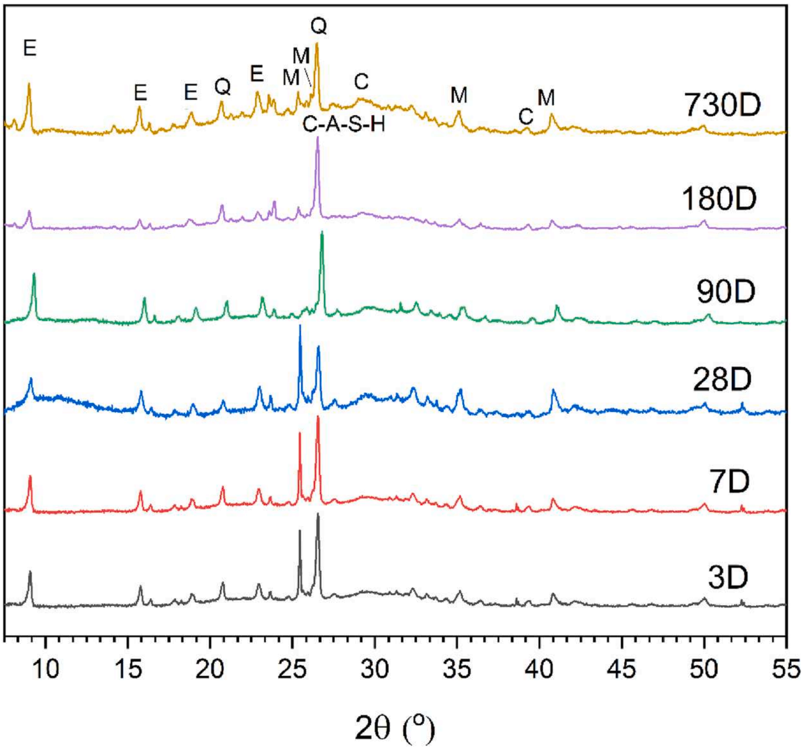

Fig. 7. X-ray diffractograms showing the phases formed within ZCC paste as a function of curing duration under sealed conditions. Identified phases are represented by E: ettringite (formed as a hydration product), M: mullite and Q: quartz (residual inert phases from the fly ash precursor), and C: calcite (formed as a minor carbonation product during curing and/or analysis). The broad feature marked (from underneath) as C-A-S-H indicates the main binding gel, which is crystallographically disordered.

within an aluminium-substituted calcium silicate hydrate (C-A-S-H) gel [42,43] (Fig. 8), consistent with previous observations for binders based on Portland cement blended with blast furnace slag, and alkali-activated slag cements [44-46].

A broad resonance due to Q^0 Si sites in unreacted anhydrous slag also contributes to the spectra for each sample at $\delta_{iso}= -70$ ppm. Another broad resonance is observed at $\delta_{iso}= -110$ ppm and is attributed to Q^4 Si sites in unreacted anhydrous fly ash and silica fume. Due to extensive overlap between the resonances of the raw material and reaction product peaks, and the limited signal/noise ratio achieved in the spectra due to the iron content of the fly ash, it has not been possible to conduct any quantitative analysis of these spectra, but qualitative discussion of the observed features nonetheless remains instructive.

There is little change in these spectra when comparing samples of different curing ages, indicating that the local Si environment does not change significantly with time during curing. Samples aged for longer curing periods exhibit greater intensity in the region of the spectra attributed to Q^2 sites, showing increased formation of C-A-S-H with time. Some intensity is also observed at later curing ages in the region attributed to Q^3 and Q^3(1Al) Si sites ($\delta_{iso}= -85$ ppm and -90 ppm, respectively), indicating that increased gel crosslinking occurs as samples age. There is some residual silica fume at -115 to -120 ppm in the 3 d spectrum [46], overlaid as a shoulder on the larger FA peak; this persists to some degree up to 90 d, but is greatly reduced at 730 d

Fig. 9 shows the ^{27}Al MAS NMR data for ZCC paste, cured under sealed conditions, from 3 to 730 days. The spectra contain resonance signals in the ranges of tetrahedrally coordinated Al (observed chemical shift, δ_{obs}, = 50–80 ppm), pentahedrally coordinated Al (δ_{obs} = 20–50 ppm), and octahedrally coordinated Al (δ_{obs} = −5 to 20 ppm) [47].

The broad signal located around 55–80 ppm arises due to resonances in both 4-coordinated Al in the glassy phase of unreacted FA and GGBFS [44,46,48,49], and 4-coordinated Al substituting for Si in the silicate chains of the C-A-S-H [47,49,50]. However, as these signals overlap within the same chemical shift region of the present spectra, they cannot be identified unambiguously. Nevertheless, resonances of 5-coordinated and 6-coordinated Al at approximately 40 ppm and 4–5 ppm, respectively, usually associated with C-A-S-H and assigned to the 'third aluminate hydrate' (TAH) [45,51,52] or hydrated Al in the silicate chains [53], are identified in the spectra of the cement pastes from early age onwards, confirming the formation of C-A-S-H. The ^{27}Al MAS NMR data show the formation and evolution of the C-A-S-H over time, according to the reaction mechanisms hypothesised above, evident from the shift in the main ^{27}Al resonance from 70 ppm toward 60 ppm in Fig. 9 at later age. This gives evidence for more incorporation of Al into the C-A-S-H over time as the reaction process continues to evolve and generate C-A-S-H from progressively more and more Al-rich precursors. The order of reactivity of the main solid phases (SF > BFS > FA) is the inverse of the Al contents of these precursors (FA > BFS > SF; Section 2.1), and so the C-S-H that is initially produced by pozzolanic reaction of the SF will progressively be supplanted by C-A-S-H resulting from slag hydration and then from fly ash hydration. There may also be some additional Al made available as ettringite becomes less prominent in the spectra at later age, as discussed below, but this would be expected to be an Al source of secondary importance compared to the ongoing hydration processes which were identified through porosimetry in Section 3.2. The growth in Al incorporation is also consistent with the formation of the extra side-peak in the ^{29}Si MAS NMR spectra (Fig. 8) at −80 ppm, which is assigned to the presence of Al-substituted chains in the C-A-S-H.

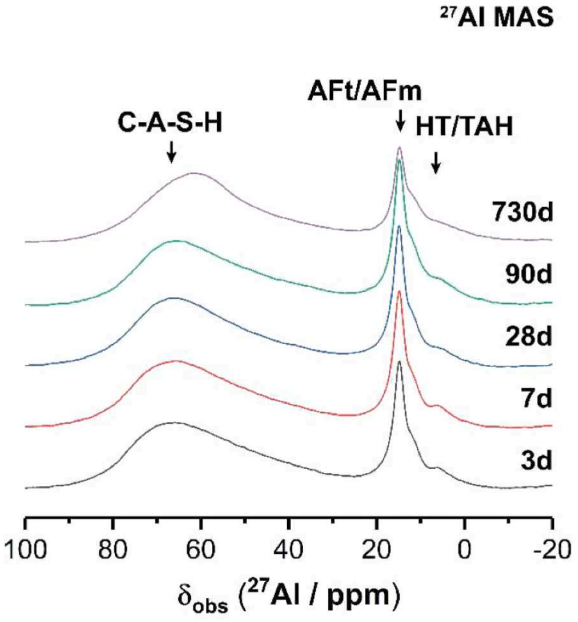

Fig. 9. ^{27}Al MAS NMR spectra of ZCC pastes, as a function of sealed curing duration; includes some data from [10].

The 4- and 6-coordinated Al sites in mullite are characterised by resonances at 45–50 ppm and 0 to −5 ppm, respectively [54,55]; however, these resonances cannot be identified unambiguously in the spectra due to the low content of mullite in the cements (as identified by the weak XRD peaks corresponding to this phase in Fig. 7), and also the tendency of mullite in residual fly ash grains to contain significant Fe substitution onto Al sites [56], which suppresses the measured NMR signal of nearby Al sites [57].

In addition to the resonance of 6-coordinated Al in C-A-S-H, the region −5 to 20 ppm contains the signals of 6-coordinated Al in AFt and AFm phases. A strong signal at approximately 15 ppm and a partly overlapping peak or shoulder at 11.8–12 ppm are present in the spectra of all cement pastes (Fig. 9). The signal at 15 ppm is attributed to ettringite, while the signal at approximately 12 ppm is generally related to AFm phases and/or Mg-Al LDH (hydrotalcite- or meixnerite-type phases) in hydrated cements [47,58,59]. The continuing hydration of the BFS causes growth in the Mg-Al LDH resonance, consistent with the SEM images that show this as part of the concentric ring structure around BFS grains (Section 3.3) [15]. The presence of ettringite in the cement pastes was shown by XRD analysis; however, unequivocal evidence of AFm phases was not found in the XRD patterns (Fig. 7). The formation of AFt is largely completed within the first 3 days of reaction, consistent with the discussion in Section 3.4 regarding early-age depletion of the sulfate provided by the expansive additive. The sharp peak at around 15 ppm associated with AFt decreases significantly from 90 to 730 days, consistent with the XRD data as discussed in Section 3.4; this may be a secondary source for the extra Al identified to have entered the C-A-S-H phase at this later age.

SR-FTIR microscopy, Fig. 10, has additionally been used to probe the binder chemical structure in a spatially-resolved manner, aiming to identify gel structural features at the interface between the FNS aggregate and the paste. The scanning electron micrograph at the bottom of the composite image in Fig. 10 demonstrates the region of interest, which is also highlighted on the heat maps that correspond to specific spectral regions. This technique is relatively less familiar in the field of cement science [60,61], but is a well-established technique across many areas of materials science and related fields [62].

The area identified here for analysis is enriched in Mg and Na compared to the bulk binder, as seen from the EDX maps in Fig. 10. These elements are sourced from the FNS and their presence within the gel is consistent with the discussion above regarding the reactivity of the aggregate surface. There are few regions of localized high Ca content; the calcium distribution within the region is relatively uniform other than in the small region identified as calcium carbonate which is at the upper-left of the region marked in red in the SEM image. The several isolated regions of high Si and Al content that do not correspondingly have high Ca are identified as residual fly ash grains; these are not all

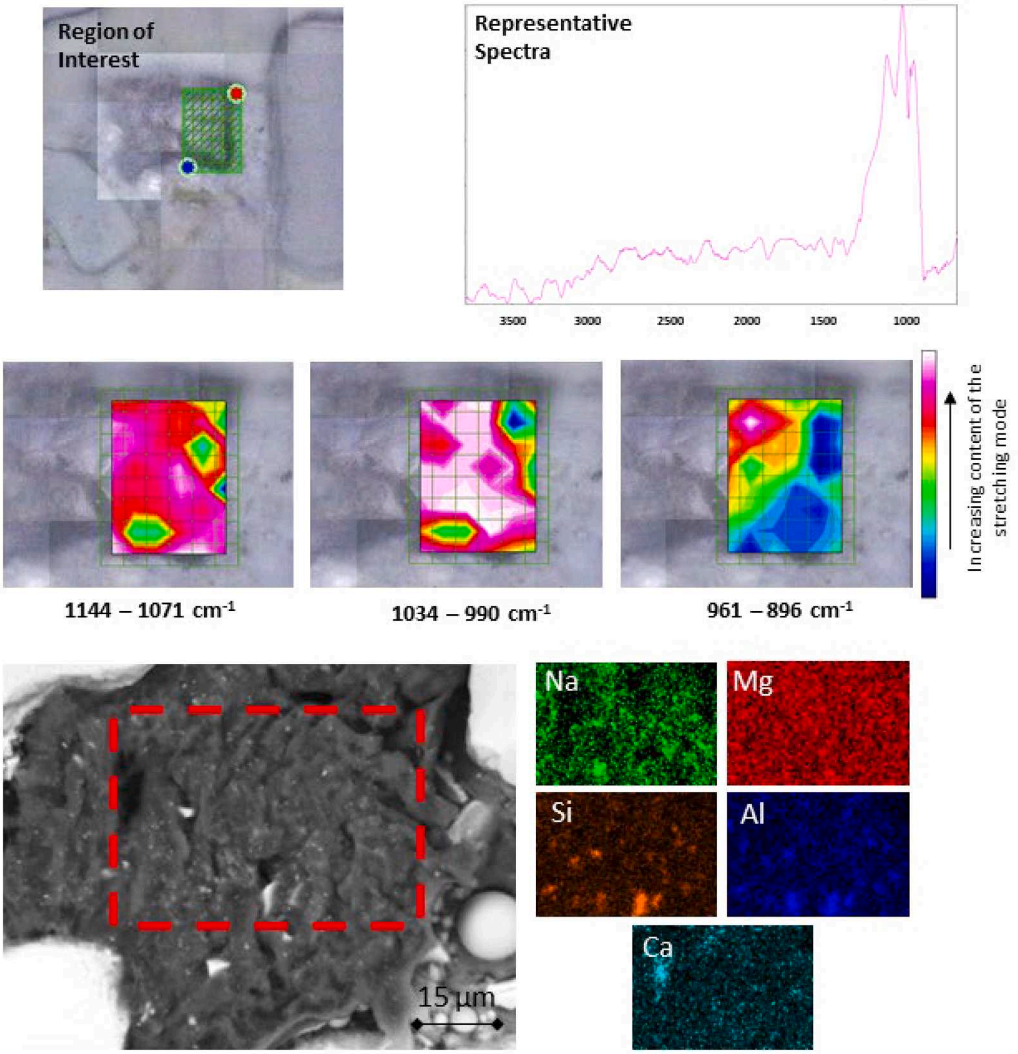

Fig. 10. SR-FTIR microscopy applied to the study of a region of interest on a ZCC mortar after 360 days of 20 °C curing (optical micrograph at top), identified by the red box in the SEM image and EDX maps shown at the bottom of the image. The SR-FTIR integral maps in the centre of the image highlight the formation of distinct reaction products consistent with C-A-S-H and LDH phases, as described in the text.

directly visible in the SEM image or in the FTIR spectra, but can be detected by EDX due to the probe depth of several microns that applies specifically to this technique when applied to cement binders with modest calcium content [63], as is the case here.

The spectral regions of interest shown in Fig. 10 are selected to relate to the known FTIR spectral features of cementitious hydrate products, particularly C-A-S-H, and are mapped to show the integrated spectral intensity in each selected wavenumber range at each analysis point. This method of analysis is dependent on the availability of a flat, optically reflective region on the sample surface, which is the case for the region shown here, other than maybe a sub-region at the bottom left of the maps shown in Fig. 9 where the intensities of all signals drop, indicating a partial loss of sample flatness. The interfacial binding phase has strong responses within the regions of 1144 – 1071 cm^{-1}, 1034 – 990 cm^{-1}, and 961 – 896 cm^{-1}, each of which is mapped in Fig. 10. Ettringite is known to have a very strong infrared absorption band at 1100–1130 cm^{-1} due to vibrations within the sulfate anion in its structure [64], while the vibrations of C-S-H and C-A-S-H are most intense at wavenumbers below 960 cm^{-1} at high Ca/Si ratio and/or high Al content, increasing to show significant intensity around 1000 cm^{-1} at lower Ca/Si ratios and in the absence of Al [65,66]. Hydrotalcite-group Mg/Al-LDH phases have been observed to show a very broad FTIR signal in this region, decreasing gradually with increasing wavenumber across the range 800–1200 cm^{-1} [67], and so would not be expected to be identified specifically in any of the maps shown in Fig. 10.

From this basis, the mapping results can be used to identify that the gel regions close to the FNS aggregate particles mainly consist of C-A-S-H with low Ca/Si ratio and/or significant Al content; both SF and BFS have evidently participated in the formation of this phase. Further from the aggregate surface, a region that appears to be enriched in ettringite is shown (top left of the mapped regions in Fig. 10), identified by its stronger signal at higher wavenumber. The high-wavenumber map shows a relatively high and uniform signal across the rest of the mapped region, which may also reflect the presence of unreacted silica fume particles that would also show an absorption band in this spectral region, consistent with the NMR analysis above. The intermixing of these phases takes place on a length scale finer than the spatial resolution of either the infrared or electron microscopy techniques applied here, but the multi-spectral mapping provides useful insight into the spatial distribution of both elements and chemical structural features within the binders.

4. Discussion

Through the examination of the ZCC paste and mortar samples, it has been identified that the high strength observed for ZCC is due to a combination of the following factors (in likely order of importance):

- Very low water content.
- The Ca provided by the expansive additive appears to activate the paste, in a similar way to alkali activated slag and the pozzolanic reaction of SF, and therefore produce a continuously reacting C-A-S-H gel. The activation of the SF prior to reaction of the BFS leads to the production of initial C-A-S-H, which provides a surface upon which the production of further C-A-S-H binding phases can take place.
- Formation of a C-A-S-H gel network within the microstructure that allows for an ongoing reaction of the embedded SF, slag, and fly ash grains, leading to further densification, through the production of additional hydrate phases. This proceeds despite the low water content and limited free space available for reaction, because the C-A-S-H develops extensively in outer product regions so does not block the particle surfaces; this behavior may also be related to the low bound water content and high dimensional stability of the binding phase assemblages formed.
- The very low porosity of ZCC results from the combination of the production of a large amount of C-A-S-H, porosity being filled by ettringite, and also the very low free water content which is enabled by the high superplasticiser dose used.
- The reactivity of the FNS aggregate contributes significantly to the development of a high tensile strength in particular; the combination of this with a micro-aggregate effect from unreacted fly ash grains is very beneficial in this regard. There is a strong adhesion between the aggregate and paste, without evidence of deleterious alkali-aggregate processes.

The stability and compatibility of the hydration product assemblages produced is expected to be excellent. These binders are based on C-A-S-H and ettringite, and also including some hydrotalcite-group Mg-Al LDH phases. These are well known to be stable in conjunction with each other, in various cementitious phase assemblages that have been computed through thermodynamic modelling [68,69] and in numerous experimental studies. There is a tendency in modern cement science to also use results obtained for ancient Roman lime-pozzolan cements to justify predictions of durability across a wide range of binder formulations. In the case of the materials here, which are actually largely produced via lime-pozzolan reactions, connections to studies such as [70] which highlight C-A-S-H as a durable and resilient binding phase in such materials can provide further confidence in the long-term engineering performance of ZCC. The presence of a partially-reactive fine aggregate here also offers a further parallel to the analysis of Seymour et al. [71] who have recently discussed the benefits provided by a reactive volcanic aggregate in combination with lime-pozzolan binders to form C-A-S-H in an ancient concrete that they described as “robust” and “highly cohesive”. Ongoing engineering properties tests are nonetheless needed to demonstrate the in-service performance of ZCC in the longer term, and particularly with regard to the eventual fate of the superplasticiser molecules.

5. Conclusions

This study has provided chemical and microstructural characterisation of a Portland cement-free high-performance binder and mortar, which is produced by chemical activation of a ternary silica fume-blast furnace slag-fly ash blend using a CaO-rich expansive additive. The very low water/cement ratio (enabled by triggered release of a superplasticiser from the silica fume grains as analysed previously) and partially reactive nature of the ferronickel slag sand used as fine aggregate combine to give a binder which has very low porosity and high strength in both compression and tension. The binder structure is dominated by C-A-S-H that forms initially (as C-S-H) through reaction of silica fume with CaO, in regions that would be identified as “outer product” space, well away from the surfaces of BFS grains, which enables the ongoing later hydration of BFS to form a dense and space-filling microstructure. Ettringite and aluminate layered double hydroxides form as additional hydration products, intimately intermixed with the C-A-S-H. Overall the binder structure that is formed in these Portland cement-free materials is comprised of similar binding phases to those which are developed through hydration of Portland cement in the presence of conventional supplementary cementitious materials, with a dense microstructure and very high ongoing strength development beyond 28 days, which offers an attractive combination of engineering properties and the likelihood of high chemical durability in service.

CRediT authorship contribution statement

Daniel A. Geddes: Writing – review & editing, Methodology, Investigation. **Brant Walkley:** Writing – review & editing, Visualization, Methodology, Investigation, Funding acquisition, Formal analysis. **Taku Matsuda:** Writing – review & editing, Supervision, Resources, Project administration, Methodology, Investigation, Funding acquisition, Conceptualization. **John L. Provis:** Writing – review & editing, Writing – original draft, Visualization, Supervision, Resources, Project administration, Methodology, Investigation, Funding acquisition, Conceptualization.

Declaration of competing interest

The authors declare the following financial interests/personal relationships which may be considered as potential competing interests:

John Provis and Brant Walkley report financial support was provided by Sumitomo Mitsui Construction Co Ltd. Taku Matsuda reports a relationship with Sumitomo Mitsui Construction Co Ltd that includes: employment.

Data availability

Data will be made available on request.

Acknowledgements

This study has been funded by Sumitomo Mitsui Construction Co. Ltd., Japan, through a grant to BW and JLP. We wish to thank and acknowledge Dr Sandra van Meurs and Dr Khalid Doudin, Department of Chemistry, The University of Sheffield, for assistance in acquiring the NMR data and insightful discussions related to this work. We thank and acknowledge Dr Gianfelice Cinque, Diamond Light Source, for his excellent support in operating the synchrotron FTIR instrument in remote-control mode during Covid19 restrictions. We also would like to thank Dr Oday Hussein, Henry Royce Institute, University of Sheffield, for assistance in data acquisition using the facilities of that institute.

References

[1] G. Habert, S.A. Miller, V.M. John, J.L. Provis, A. Favier, A. Horvath, K.L. Scrivener, Environmental impacts and decarbonization strategies in the cement and concrete industries, Nat. Rev. Earth Environ. 1 (2020) 559–573.

[2] I.L. Larsen, I. Granseth Aasbakken, R. O'Born, K. Vertes, R.T. Thorstensen, Determining the environmental benefits of ultra high performance concrete as a bridge construction material, IOP Confer. Ser. Mater. Sci. Eng. 245 (2017) #052096.

[3] X. Wang, D. Wu, J. Zhang, R. Yu, D. Hou, Z. Shui, Design of sustainable ultra-high performance concrete: a review, Constr. Build. Mater. 307 (2021) #124643.

[4] P. Purnell, Material nature versus structural nurture: the embodied carbon of fundamental structural elements, Environ. Sci. Technol. 46 (2011) 454–461.

[5] T. Matsuda, T. Noguchi, M. Kanematsu, R. Mine, Ultralow shrinkage and high strength concrete without Portland cement, in: Better, Smarter, Stronger - Proceedings of the 5th *fib* Congress, fib, Melbourne, Australia, 2018.

[6] W. Sasaki, T. Matsuda, R. Mine, Y. Onda, Development of high strength fiber reinforced concrete without Portland cement, in: W. Derkowski, P. Krajewski, P. Gwozdziewicz, M. Pantak (Eds.), Concrete Innovations in Materials, Design and Structures - Proceedings of the 16th *fib* Symposium, fib, Krakow, Poland, 2019.

[7] T. Matsuda, D.A. Geddes, B. Walkley, J.L. Provis, Properties and hardening mechanism of ultralow shrinkage and high strength zero-cement-concrete, in: B. Zhao, X. Lu (Eds.) Concrete Structures for Resilient Society - Proceedings of the 17th *fib* Symposium 2020, fib, Shanghai, China, 2020.

[8] T. Matsuda, High-performance concrete that achieve ultra-low shrinkage, low carbon, low heat generation, high strength, and high fluidity using by-products, Concr. J. (JCI) 59 (2021) 788–793.

[9] T. Matsuda, R. Sakamoto, D.A. Geddes, B. Walkley, J.L. Provis, An experimental study on shrinkage and mechanical properties of ultra-low shrinkage and high strength Zero-Cement Concrete, in: E. Júlio, J. Valença, A.S. Louro (Eds.), Concrete Structure: New Trends For Eco-Efficiency and Performance - Proceedings of the 18th *fib* Symposium, fib, Lisbon, Portugal, 2021.

[10] T. Matsuda, R. Mine, D.A. Geddes, B. Walkley, J.L. Provis, Development of ultra-low shrinkage and high strength concrete without Portland cement with experimental study on its fabrication, in: S. Stokkeland, H.C. Braarud (Eds.), Concrete Innovation for Sustainability - Proceedings of the 6th *fib* International Congress, fib, Oslo, Norway, 2022.

[11] H. Shinozaki, A. Kasuga, T. Matsuda, Construction of non-metallic bridge using zero-cement concrete, in: S. Stokkeland, H.C. Braarud (Eds.), Concrete Innovation for Sustainability - Proceedings of the 6th *fib* International Congress, fib, Oslo, Norway, 2022.

[12] B. Walkley, D.A. Geddes, T. Matsuda, J.L. Provis, Reversible adsorption of polycarboxylates on silica fume in high pH, high ionic strength environments for control of concrete fluidity, Langmuir. 38 (2022) 1662–1671.

[13] W. Sasaki, Going cement-free, Bd&e 96 (2019) 64–65.

[14] H. Shinozaki, W. Sasaki, T. Sanga, T. Matsuda, Trial of PC bridge in pursuit of sustainability, Concr. J. (JCI) 59 (2021) 511–518.

[15] R. San Nicolas, S.A. Bernal, R. Mejía de Gutiérrez, J.S.J. van Deventer, J.L. Provis, Distinctive microstructural features of aged sodium silicate activated slag concretes,, Cem. Concr. Res. 65 (2014) 41–51.

[16] B.S. Gebregziabiher, R. Thomas, S. Peethamparan, Very early-age reaction kinetics and microstructural development in alkali-activated slag, Cem. Concr. Compos. 55 (2015) 91–102.

[17] M. Ben Haha, G.Le Saout, F. Winnefeld, B. Lothenbach, Influence of activator type on hydration kinetics, hydrate assemblage and microstructural development of alkali activated blast-furnace slags,, Cem. Concr. Res. 41 (2011) 301–310.

[18] J. Seo, S. Park, H.N. Yoon, H.K. Lee, Effect of CaO incorporation on the microstructure and autogenous shrinkage of ternary blend Portland cement-slag-silica fume, Constr. Build. Mater. 249 (2020) #118691.

[19] G. Cinque, M. Frogley, K. Wehbe, J. Filik, J. Pijanka, Multimode InfraRed Imaging and Microspectroscopy (MIRIAM) beamline at Diamond, Synchrotron Radiat. News 24 (2011) 24–33.

[20] T.C. Powers, T.L. Brownyard, Studies of the physical properties of hardened Portland cement paste. Part 6. Relation of physical characteristics of the paste to compressive strength, J. Am. Concr. Inst. 43 (1947) 845–864.

[21] H. Brouwers, The work of Powers and Brownyard revisited: part 1, Cem. Concr. Res. 34 (2004) 1697–1716.

[22] B. Pichler, C. Hellmich, J. Eberhardsteiner, J. Wasserbauer, P. Termkhajornkit, R. Barbarulo, G. Chanvillard, Effect of gel–space ratio and microstructure on strength of hydrating cementitious materials: An engineering micromechanics approach, Cem. Concr. Res. 45 (2013) 55–68.

[23] D.P. Bentz, P.V. Coveney, E.J. Garboczi, M.F. Kleyn, P.E. Stutzman, Cellular automation simulations of cement hydration and microstructure development, Model. Simul. Mater. Sci. Eng. 2 (1994) 783–808.

[24] J.W. Bullard, H.M. Jennings, R.A. Livingston, A. Nonat, G.W. Scherer, J. S. Schweitzer, K. Scrivener, J.J. Thomas, Mechanisms of cement hydration, Cem. Concr. Res. 41 (2011) 1208–1223.

[25] J.E. Vigor, S.A. Bernal, X. Xiao, J.L. Provis, Time-resolved 3D characterisation of early-age microstructural development of Portland cement, J. Mater. Sci. 57 (2022) 4952–4969.

[26] T. Noguchi, F. Tomosawa, Relationship between compressive strength and various mechanical properties of high strength concrete, J. Struct. Constr. Eng. (Trans. AIJ) 60 (1995) 11–16.

[27] T. Noguchi, F. Tomosawa, Relationship between compressive strength and modulus of elasticity of high strength concrete, J. Struct. Constr. Eng. (Trans. AIJ) 60 (1995) 1–10.

[28] I. Schachinger, T. Stengel, H. Hilbig, Effect of curing temperature at an early age on the long-term strength development of UHPC, in: E. Fehling, M. Schmidt, S. Stürwald (Eds.), Proceedings of the Second International Symposium on Ultra High Performance Concrete, Kassel University Press, Kassel, Germany, 2008, pp. 205–212.

[29] Y. Jeong, H. Park, Y. Jun, J.-H. Jeong, J.E. Oh, Microstructural verification of the strength performance of ternary blended cement systems with high volumes of fly ash and GGBFS, Constr. Build. Mater. 95 (2015) 96–107.

[30] E.R. Grist, K.A. Paine, A. Heath, J. Norman, H. Pinder, Structural and durability properties of hydraulic lime–pozzolan concretes, Cem. Concr. Res. 62 (2015) 212–223.

[31] Q.D. Nguyen, M.S.H. Khan, T. Xu, A. Castel, Mitigating the risk of early age cracking in fly ash blended cement-based concrete using ferronickel slag sand, J. Adv. Concr. Technol. 17 (2018) 295–308.

[32] J. Bao, Z. Yu, L. Wang, P. Zhang, X. Wan, S. Gao, T. Zhao, Application of ferronickel slag as fine aggregate in recycled aggregate concrete and the effects on transport properties, J. Clean. Prod. 304 (2021) #127149.

[33] A.K. Saha, P.K. Sarker, Expansion due to alkali-silica reaction of ferronickel slag fine aggregate in OPC and blended cement mortars, Constr. Build. Mater. 123 (2016) 135–142.

[34] B. Li, Q. Li, W. Chen, Spatial zonation of a hydrotalcite-like phase in the inner product of slag: new insights into the hydration mechanism, Cem. Concr. Res. 145 (2021) #106460.

[35] S.A. Kearney, E. Tajuelo Rodriguez, J.D. Arregui-Mena, S.M. Lawson, J.L. Provis, Simulation of radiation damage via alpha decay in BFS:PC grouts using $^{4}He^{2+}$ ion acceleration, Cem. Concr. Res. 159 (2022) 106895.

[36] A. Arora, M. Aguayo, H. Hansen, C. Castro, E. Federspiel, B. Mobasher, N. Neithalath, Microstructural packing- and rheology-based binder selection and characterization for ultra-high performance concrete (UHPC), Cem. Concr. Res. 103 (2018) 179–190.

[37] A.K.H. Kwan, J.J. Chen, Adding fly ash microsphere to improve packing density, flowability and strength of cement paste, Powder Technol. 234 (2013) 19–25.

[38] Q. Wang, D. Wang, H. Chen, The role of fly ash microsphere in the microstructure and macroscopic properties of high-strength concrete, Cem. Concr. Res. 83 (2017) 125–137.

[39] K.L. Scrivener, A.K. Crumbie, P. Laugesen, The interfacial transition zone (ITZ) between cement paste and aggregate in concrete, Interf. Sci. 12 (2004) 411–421.

[40] R. San Nicolas, J.L. Provis, The interfacial transition zone in alkali-activated slag mortars, Front. Mater. 2 (2015) #70.

[41] Z. Luo, W. Li, K. Wang, S.P. Shah, D. Sheng, Nano/micromechanical characterisation and image analysis on the properties and heterogeneity of ITZs in geopolymer concrete, Cem. Concr. Res. 152 (2022) #106677.

[42] I.G. Richardson, A.R. Brough, R. Brydson, G.W. Groves, C.M. Dobson, Location of aluminum in substituted calcium silicate hydrate (C-S-H) gels as determined by ^{29}Si and ^{27}Al NMR and EELS, J. Am. Ceram. Soc. 76 (1993) 2285–2288.

[43] Z. Dai, T.T. Tran, J. Skibsted, Aluminum incorporation in the C–S–H phase of white Portland cement–metakaolin blends studied by ^{27}Al and ^{29}Si MAS NMR spectroscopy, J. Am. Ceram. Soc. 97 (2014) 2662–2671.

[44] S.A. Bernal, J.L. Provis, B. Walkley, R. San Nicolas, J.D. Gehman, D.G. Brice, A. R. Kilcullen, P. Duxson, J.S.J. van Deventer, Gel nanostructure in alkali-activated binders based on slag and fly ash, and effects of accelerated carbonation, Cem. Concr. Res. 53 (2013) 127–144.

[45] R.J. Myers, S.A. Bernal, J.L. Provis, J.D. Gehman, J.S.J. van Deventer, The role of Al in cross-linking of alkali-activated slag cements, J. Am. Ceram. Soc. 98 (2015) 996–1004.

[46] K.L. Scrivener, B. Lothenbach, N. De Belie, E. Gruyaert, J. Skibsted, R. Snellings, A. Vollpracht, TC 238-SCM: hydration and microstructure of concrete with SCMs. State of the art on methods to determine degree of reaction of SCMs, Mater. Struct. 48 (2015) 835–862.

[47] B. Walkley, J.L. Provis, Solid-state nuclear magnetic resonance spectroscopy of cements, Mater. Today Adv. 1 (2019) #100007.

[48] O. Burciaga-Díaz, J.I. Escalante-García, Structure, mechanisms of reaction, and strength of an alkali-activated blast-furnace slag, J. Am. Ceram. Soc. 96 (2014) 3939–3948.

[49] S. Murgier, H. Zanni, D. Gouvenot, Blast furnace slag cement: a ^{29}Si and ^{27}Al NMR study, C. R. Chimie 7 (2004) 389–394.

[50] J. Skibsted, M.D. Andersen, The effect of alkali ions on the incorporation of aluminum in the calcium silicate hydrate (C–S–H) phase resulting from Portland cement hydration studied by ^{29}Si MAS NMR, Journal of the American Ceramic Society 96 (2013) 651–656.

[51] M.D. Andersen, H.J. Jakobsen, J. Skibsted, A new aluminium-hydrate species in hydrated Portland cements characterized by ^{27}Al and ^{29}Si MAS NMR spectroscopy, Cem. Concr. Res. 36 (2006) 3–17.

[52] G. Renaudin, J. Russias, F. Leroux, C. Cau-dit-Comes, F. Frizon, Structural characterization of C-S-H and C-A-S-H samples - Part II: local environment investigated by spectroscopic analyses, J. Solid State Chem. 182 (2009) 3320–3329.

[53] A. Kunhi Mohamed, P. Moutzouri, P. Berruyer, B.J. Walder, J. Siramanont, M. Harris, M. Negroni, S.C. Galmarini, S.C. Parker, K.L. Scrivener, L. Emsley, P. Bowen, The atomic-level structure of cementitious calcium aluminate silicate hydrate, J. Am. Chem. Soc. 142 (2020) 11060–11071.

[54] J. Sanz, A. Madani, J.M. Serratosa, J.S. Moya, S. Aza, Aluminum-27 and silicon-29 magic-angle spinning nuclear magnetic resonance study of the kaolinite-mullite transformation, J. Am. Ceram. Soc. 71 (1988) C418–C421.

[55] H. He, J. Guo, J. Zhu, P. Yuan, C. Hu, ^{29}Si and ^{27}Al MAS NMR spectra of mullites from different kaolinites, Spectrochim. Acta Part A: Mol. Biomol. Spectr. 60 (2004) 1061–1064.

[56] S. Gomes, M. François, Characterization of mullite in silicoaluminous fly ash by XRD, TEM, and ^{29}Si MAS NMR, Cem. Concr. Res. 30 (2000) 175–181.

[57] D.L. Carroll, T.F. Kemp, T.J. Bastow, M.E. Smith, Solid-state NMR characterisation of the thermal transformation of a Hungarian white illite, Solid State Nucl. Magn. Reson. 28 (2005) 31–43.

[58] J. Skibsted, E. Henderson, H.J. Jakobsen, Characterization of calcium aluminate phases in cements by ^{27}Al MAS NMR spectroscopy, Inorg. Chem. 32 (1993) 1013–1027.

[59] M.R. Jones, D.E. Macphee, J.A. Chudek, G. Hunter, R. Lannegrand, R. Talero, S. N. Scrimgeour, Studies using ^{27}Al MAS NMR of AFm and AFt phases and the formation of Friedel's salt, Cem. Concr. Res. 33 (2003) 177–182.

[60] A. Hajimohammadi, J.L. Provis, J.S.J. van Deventer, Time-resolved and spatially-resolved infrared spectroscopic observation of seeded nucleation controlling geopolymer gel formation, J. Colloid Interface Sci. 357 (2011) 384–392.

[61] J.L. Provis, A. Hajimohammadi, C.E. White, S.A. Bernal, R.J. Myers, R.P. Winarski, V. Rose, T.E. Proffen, A. Llobet, J.S.J. van Deventer, Nanostructural characterization of geopolymers by advanced beamline techniques, Cem. Concr. Compos. 36 (2013) 56–64.

[62] H.A. Bechtel, S.C. Johnson, O. Khatib, E.A. Muller, M.B. Raschke, Synchrotron infrared nano-spectroscopy and -imaging, Surf. Sci. Rep. 75 (2020) #100493.

[63] R.R. Lloyd, J.L. Provis, J.S.J. van Deventer, Microscopy and microanalysis of inorganic polymer cements. 1: remnant fly ash particles, J. Mater. Sci. 44 (2009) 608–619.

[64] E. Scholtzová, L. Kucková, J. Kožíšek, D. Tunega, Structural and spectroscopic characterization of ettringite mineral – combined DFT and experimental study, J. Mol. Struct. 1100 (2015) 215–224.

[65] P. Yu, R.J. Kirkpatrick, B. Poe, P.F. McMillan, X. Cong, Structure of calcium silicate hydrate (C-S-H): near-, mid-, and far-infrared spectroscopy, J. Am. Ceram. Soc. 82 (1999) 742–748.

[66] E. Kapeluszna, Ł. Kotwica, A. Różycka, Ł. Gołek, Incorporation of Al in C-A-S-H gels with various Ca/Si and Al/Si ratio: microstructural and structural characteristics with DTA/TG, XRD, FTIR and TEM analysis, Constr. Build. Mater. 155 (2017) 643–653.

[67] J.T. Kloprogge, D. Wharton, L. Hickey, R.L. Frost, Infrared and Raman study of interlayer anions CO_3^{2-}, NO_3^-, SO_4^{2-} and ClO_4^- in Mg/Al-hydrotalcite, Am. Mineralog. 87 (2002) 623–629.

[68] R.J. Myers, S.A. Bernal, J.L. Provis, Phase diagrams for alkali-activated slag binders, Cem. Concr. Res. 95 (2017) 3038.

[69] D.P. Prentice, B. Walkley, S.A. Bernal, M. Bankhead, M. Hayes, J.L. Provis, Thermodynamic modelling of BFS-PC cements under temperature conditions relevant to the geological disposal of nuclear wastes, Cem. Concr. Res. 119 (2019) 21–35.

[70] M.D. Jackson, E.N. Landis, P.F. Brune, M. Vitti, H. Chen, Q. Li, M. Kunz, H.-R. Wenk, P.J.M. Monteiro, A.R. Ingraffea, Mechanical resilience and cementitious processes in Imperial Roman architectural mortar, Proc. Natl. Acad. Sci. 111 (2014) 18484–18489.

[71] L.M. Seymour, N. Tamura, M.D. Jackson, A. Masic, Reactive binder and aggregate interfacial zones in the mortar of Tomb of Caecilia Metella concrete, 1C BCE, Rome, J. Am. Ceram. Soc. 105 (2022) 1503–1518.